Supplementary Information

Supplementary Note 1 - Geological setting and petrological background. The Neogene Volcanic Province of southeast Spain is an ore-productive volcanic belt extending NE-SW for ~ 150 km along the Mediterranean coast. It hosts several epithermal auriferous (Roadalquilar-Carboneras) and Pb-Zn-Cu-(Ag) polymetallic (Mazarrón-La Unión district) ore deposits associated with medium- to high-K calc-alkaline volcanic episodes at ~ 9-11 Ma (Arribas et al., 1995; Milot et al., 2022). The calc-alkaline volcanism in the region began in response to the westward rollback migration of the Tethyan subduction front beneath the Alborán micro-continent (Duggen et al., 2004), which caused lateral tearing of the Iberian continental margin along subduction transform edge propagator fault systems (STEP; Mancilla et al., 2015). The shift towards high-K, shoshonitic, and lamproite magmatism since the Late Miocene occurred in response to continental edge delamination of the Iberian lithosphere, which drove asthenosphere upwelling and melting of metasomatized domains of the subcontinental lithospheric mantle (SCLM; Duggen et al., 2005). The last stages of magmatism in the area involved the extrusion of intra-plate type alkaline basalts (6.3-0.65 Ma) (Duggen et al., 2005), which rapidly brought to the surface abundant xenoliths sampling the metasomatized SCLM that previously fed the ore-productive volcanism of the region (Hidas et al., 2016; Marchesi et al., 2017; Dallai et al., 2019; Avanzinelli et al., 2020; Schettino et al., 2022).

The studied nanoparticle-bearing peridotite xenoliths come from the Tallante volcanic field, and represent a volume of fertile SCLM that experienced metal endowment through the crystallization of precious metal-rich nanoparticles incorporated in metasomatic sulfides (González-Jiménez et al., 2020; Schettino et al., 2022). The targeted xenoliths have a medium-to-fine grained (0.5-2 mm) granular texture characterized by the presence of olivine porphyroclasts in a granoblastic matrix of poorly strained olivine neoblasts and amoeboid orthopyroxene,

clinopyroxene and spinel. The major element compositions of the rock-forming minerals record cooling and decompression of this portion of lithospheric mantle from 1100 °C at 1.8-1.9 GPa to 850 °C at 0.7-0.9 GPa (Rampone et al., 2010; Hidas et al., 2016). The estimated fO_2 conditions based on the olivine-spinel oxybarometer (Ballhaus et al., 1991) vary between -1.5 to +1.5 relative to the fayalite-magnetite-quartz buffer (FMQ), which fall within the range typically observed in a subduction-metasomatized lithospheric mantle (Bénard et al., 2018). Spherical droplets of base-metal sulfides enriched in metals (Au ~ 1.78 ppm) up to 20-50 μm across (González-Jiménez et al., 2020; Schettino et al., 2022) are systematically enclosed within metasomatic clino and orthopyroxene. The trace element signatures of sulfide-bearing clinopyroxene record silicate metasomatism by Miocene subalkaline subduction-related magmas (Schettino et al., 2022).

Lamproite dykes and lava flows extruded in this region ca. 9.3-7.1 (Pérez-Valera et al., 2013) along the STEP faults that accommodated the lateral tearing and edge delamination of the Iberian continental margin (Duggen et al., 2005; Cambeses et al., 2016). The major, trace element and isotopic compositions of lamproite rocks in southeast Spain point to a heterogeneous, pyroxenite-veined and metasomatized source region in the subcontinental lithospheric mantle (Duggen et al., 2005; Prelević and Foley, 2007), consistent with the lithological and geochemical characteristics preserved by the Tallante mantle xenoliths mentioned above (Bianchini et al., 2015; Marchesi et al., 2017; Avanzinelli et al., 2020; Casalini et al., 2021). The lamproite dykes from the locality of Fortuna (~ 7.71 Ma; Kuiper et al., 2006) studied here have a porphyritic texture with euhedral phenocrysts and microlites of olivine, phlogopite, orthopyroxene and apatite that are dispersed in a glassy to microcrystalline groundmass (Venturelli et al., 1988). Orthopyroxene and phlogopite phenocrysts started crystallizing at T ~1100 °C and FMQ ± 1 as multiple magma batches of lamproite melts ascended by channelized flow from the source region (~ 25-70 km depth, Fritschle et al., 2013) and mixed within localized magma chambers near the mantle-crust boundary (Cambeses et al., 2016). Base-metal sulfides in Fortuna lamproites occur as rounded droplets

included within the grain core of prismatic orthopyroxene phenocrysts (Sharygin et al., 2003), indicating that they were trapped while the lamproite melt rose from the mantle source to crustal magma chambers. Translithospheric fault systems (e.g., Socovos fault) tore down to the magma chambers during progressive delamination of the Iberian margin (Mancilla et al., 2015), and triggered the fast eruption of the lamproite magmas to the surface (Pérez-Valera et al., 2013).

Supplementary Note 2 - Physical transport of sulfide droplets in ascending lamproite magmas. Experimental work reported that sulfide liquid has high dihedral angles (θ ~150-180°) relative to a silicate melt (Mungall & Su, 2005). Therefore, sulfide liquid in silicate magmas forms isolated dispersed droplets (Wang et al., 2020), which are twice as dense (4500 kg/m^3, Mungall & Su, 2005; Kress et al., 2008) as the surrounding silicate melt (~2200-2800 kg/m^3). Such a density contrast results into negative buoyancy (i.e., gravitational settling) of the sulfide droplets, which opposes the viscous resistive forces according to the general laws of fluid dynamics and mass transfer (Clift et al., 2005). In particular, whether spherical droplets of sulfide liquid dispersed in silicate melt settle or remain entrained in the ascending magmas is determined by the difference between the vertical terminal velocity (i.e., the sinking velocity) of the sulfide droplets and the ascent rate of the host silicate magma (e.g., Heinrich and Connolly, 2022).

Small-size bubbles and droplets, such those documented in this work (< 30 μm), obey the Stokes law for a solid sphere (Clift et al., 2005) rather than the Hadamard-Rybczynski solution for liquid spheres (e.g., Robertson et al., 2015; Yao and Mungall, 2022). Therefore, we calculated the vertical terminal velocities (v) of the sulfide droplets by the Stokes law for steady creeping flow past a rigid sphere:

$$v = \frac{(\Delta\rho)}{18 * \eta} * g * d^2$$

, where g is the gravitational acceleration (9.80 m/s^2), d is the diameter of sulfide droplet (30 μm), $\Delta\rho$ the density contrast between sulfide liquid and lamproite melt, and η the temperature-dependent viscosity of lamproite melt.

The temperature-dependent viscosities (η) of the lamproite magmas were calculated with the excel calculator at https://www.eoas.ubc.ca/~krussell/VISCOSITY/grdViscosity.html (Giordano et al., 2008). Major element composition of the Fortuna lamproite magma was provided by Duggen et al. (2005), whereas an average density of 2585 kg/m^3 was adopted for a lamproite melt (Rao et al., 2008). A fixed density of 4500 kg/m^3 was used for a sulfide liquid spanning the range of major element compositions consistent with this study (Mungall & Sun, 2005; Kress et al., 2008).

The calculated settling velocities of sulfide droplets have been compared with average ascent rates of magmas within the compositional range of the lamproite melts, as well through a spectrum of subduction-related settings akin to that of the western Mediterranean in the Neogene. Estimates of ascent rates estimates of magmas vary over orders of magnitude depending on the methodological approach employed and the geological conditions through which the magmas percolate (e.g., lithospheric mantle, lower crust, upper crust). In general, U-series isotope disequilibria suggest that arc magmas rise from the supra-subduction mantle wedge to the surface with average ascent rates around 100-1000 m/yr (Turner et al., 2001; Turner and Costa, 2007). On the other hand, diffusion modelling of chemical zoning in magmatic phenocrysts point out that primitive andesitic magmas in convergent margins migrate through the lithospheric mantle and recharge crustal magma chambers with ascent rates around ~ 1000 m/day (Ruprecht and Plank, 2013). Moreover, numerical modelling of the eruption of kimberlites and similar volatile-rich magmas (e.g. lamproites) indicates that they start rising through the mantle source by rapid crack propagation due to fluid overpressure, with ascent velocities increasing from 4-50 m/s to 200-300 m/s as the propagating crack reaches the surface (Sparks et al., 2006; Wilson and Head, 2007). Taking into account these data, we suggest that the parental magmas of the Fortuna lamproite dykes

ascended from the source region in the lithospheric mantle to pre-eruption magma chambers with ascent rates ranging between 100 m/yr to 50 m/s. Despite a liquid sphere may sink up to 50% faster than a solid sphere of the same size and density, the resulting effect for sulfide droplets in our case of study would be negligible ahead of the order of magnitudes faster ascent rates of the host silicate magmas.

Supplementary References

Arribas, A., Cunningham, C. G., Rytuba, J. J., Rye, R. O., Kelly, W. C., Podwysocki, M. H., McKee, E. H., & Tosdal, R. M. (1995). Geology, geochronology, fluid inclusions, and isotope geochemistry of the Rodalquilar gold alunite deposit, Spain. *Economic Geology*, *90*(4), 795-822.

Avanzinelli, R., Bianchini, G., Tiepolo, M., Jasim, A., Natali, C., Braschi, E., Dallai, L., Beccaluva, L., & Conticelli, S. (2020). Subduction-related hybridization of the lithospheric mantle revealed by trace element and Sr-Nd-Pb isotopic data in composite xenoliths from Tallante (Betic Cordillera, Spain). *Lithos*, *352*, 105316.

Ballhaus, C., Berry, R. F., & Green, D. H. (1991). High pressure experimental calibration of the olivine-orthopyroxene-spinel oxygen geobarometer: implications for the oxidation state of the upper mantle. *Contributions to Mineralogy and Petrology*, *107*(1), 27-40.

Bénard, A., Klimm, K., Woodland, A. B., Arculus, R. J., Wilke, M., Botcharnikov, R. E., Shimizu, N., Nebel, O., Rivard, C., & Ionov, D. A. (2018). Oxidising agents in sub-arc mantle melts link slab devolatilisation and arc magmas. *Nature Communications*, *9*(1), 1-10.

Cambeses, A., Garcia-Casco, A., Scarrow, J. H., Montero, P., Pérez-Valera, L. A., & Bea, F. (2016). Mineralogical evidence for lamproite magma mixing and storage at mantle depths: Socovos fault lamproites, SE Spain. *Lithos*, *266*, 182-201.

Casalini, M., Avanzinelli, R., Tommasini, S., Natali, C., Bianchini, G., Prelević, D., Mattei, M., & Conticelli, S. (2022). Petrogenesis of Mediterranean lamproites and associated rocks: The role of overprinted metasomatic events in the post-collisional lithospheric upper mantle. *Geological Society of London Special Publications, 513,* 271-296.

Clift, R., Grace, J. R., & Weber, M. E. (2005). Bubbles, drops, and particles. Dover Publications Inc., Mineola, New York.

Dallai, L., Bianchini, G., Avanzinelli, R., Natali, C., & Conticelli, S. (2019). Heavy oxygen recycled into the lithospheric mantle. *Scientific reports*, *9*(1), 1-7.

Duggen, S., Hoernle, K., van den Bogaard, P., & Harris, C. (2004). Magmatic evolution of the Alboran region: The role of subduction in forming the western Mediterranean and causing the Messinian Salinity Crisis. *Earth and Planetary Science Letters*, *218*(1-2), 91-108.

Duggen, S., Hoernle, K., van den Bogaard, P., & Garbe-Schönberg, D. (2005). Post-collisional transition from subduction-to intraplate-type magmatism in the westernmost Mediterranean: evidence for continental-edge delamination of subcontinental lithosphere. *Journal of Petrology, 46*(6), 1155-1201.

Giordano, D., Russell, J. K., & Dingwell, D. B. (2008). Viscosity of magmatic liquids: a model. *Earth and Planetary Science Letters, 271(1-4),* 123-134.

González-Jiménez, J. M., Tassara, S., Schettino, E., Roqué-Rosell, J., Farré-de-Pablo, J., Saunders, J. E., Deditius, A. P., Colás, V., Rovira-Medina, J. J., Guadalupe-Dávalos, M. G., Schilling, M., Jimenez-Franco, A., Marchesi, C., Nieto, F., Proenza, J. A., & Gervilla, F. (2020). Mineralogy of the HSE in the subcontinental lithospheric mantle—an interpretive review. *Lithos*, *372*, 105681.

Heinrich, C. A., & Connolly, J. A. (2022). Physical transport of magmatic sulfides promotes copper enrichment in hydrothermal ore fluids. *Geology*, 50(10), 1101-1105.

Hidas, K., Konc, Z., Garrido, C.J., Tommasi, A., Vauchez, A., Padrón-Navarta, J.A., Marchesi, C., Booth-Rea, G., Acosta-Vigil, A., Szabó, C., Varas-Reus, M.I., Gervilla, F., 2016. Flow in the western Mediterranean shallow mantle: Insights from xenoliths in Pliocene alkali basalts from SE Iberia (eastern Betics, Spain). *Tectonics* 35, 2657-2676.

Kuiper, K. F., Krijgsman, W., Garcés, M., & Wijbrans, J. R. (2006). Revised isotopic (40Ar/39Ar) age for the lamproite volcano of Cabezos Negros, Fortuna basin (eastern Betics, SE Spain). *Palaeogeography, Palaeoclimatology, Palaeoecology*, *238*(1-4), 53-63.

Kress, V., Greene, L. E., Ortiz, M. D., & Mioduszewski, L. (2008). Thermochemistry of sulfide liquids IV: density measurements and the thermodynamics of O–S–Fe–Ni–Cu liquids at low to moderate pressures. Contributions to Mineralogy and Petrology, 156(6), 785-797.

Mancilla, F. d-L., Booth-Rea, G., Stich, D., Pérez-Peña, J. V., Morales, J., Azañón, J. M., Martin, R., & Giaconia, F. (2015). Slab rupture and delamination under the Betics and Rif constrained from receiver functions. *Tectonophysics*, *663*, 225-237.

Marchesi, C., Konc, Z., Garrido, C. J., Bosch, D., Hidas, K., Varas-Reus, M. I., & Acosta-Vigil, A. (2017). Multi-stage evolution of the lithospheric mantle beneath the westernmost Mediterranean: Geochemical constraints from peridotite xenoliths in the eastern Betic Cordillera (SE Spain). *Lithos*, *276*, 75-89.

Milot, J., Blichert-Toft, J., Sanz, M. A., Malod-Dognin, C., Télouk, P., & Albarède, F. (2022). Silver isotope and volatile trace element systematics in galena samples from the Iberian Peninsula and the quest for silver sources of Roman coinage. *Geology*, *50*(4), 422-426.

Mungall, J. E., & Su, S. (2005). Interfacial tension between magmatic sulfide and silicate liquids: Constraints on kinetics of sulfide liquation and sulfide migration through silicate rocks. *Earth and Planetary Science Letters, 234(1-2),* 135-149.

Pérez-Valera, L. A., Rosenbaum, G., Sánchez-Gómez, M., Azor, A., Fernández-Soler, J. M., Pérez-Valera, F., & Vasconcelos, P. M. (2013). Age distribution of lamproites along the Socovos Fault (southern Spain) and lithospheric scale tearing. *Lithos*, *180*, 252-263.

Prelević, D., & Foley, S. F. (2007). Accretion of arc-oceanic lithospheric mantle in the Mediterranean: evidence from extremely high-Mg olivines and Cr-rich spinel inclusions in lamproites. Earth and Planetary Science Letters, 256(1-2), 120-135.

Rampone, E., Vissers, R. L. M., Poggio, M., Scambelluri, M., & Zanetti, A. (2010). Melt migration and intrusion during exhumation of the Alboran lithosphere: the Tallante mantle xenolith record (Betic Cordillera, SE Spain). *Journal of Petrology*, *51*(1-2), 295-325.

Rao, N. C., Kamde, G. D., Kale, H. S., & Dongre, A. (2008). Geological setting and petrographic diversity of the lamproite dykes at the Northern and North eastern margin of the Cuddapah basin, southern India. *In Indian Dykes: Geochemistry, Geophysics and Geochronology (pp. 281-290)*. Narosa Publishing House Pvt. Ltd. New Delhi.

Robertson, J. C., Barnes, S. J., & Le Vaillant, M. (2015). Dynamics of magmatic sulphide droplets during transport in silicate melts and implications for magmatic sulphide ore formation. *Journal of Petrology*, *56(12),* 2445-2472.

Ruprecht, P., & Plank, T. (2013). Feeding andesitic eruptions with a high-speed connection from the mantle. *Nature*, *500(7460)*, 68-72.

Schettino, E., Marchesi, C., González-Jiménez, J. M., Saunders, E., Hidas, K., Gervilla, F., & Garrido, C. J. (2022). Metallogenic fingerprint of a metasomatized lithospheric mantle feeding

gold endowment in the western Mediterranean basin. *Geological Society of America Bulletin, 134*(5-6), 1468-1484.

Sharygin, V. V., Pospelova, L. N., Smirnov, S. Z., & Vladykin, N. V. (2003). Ni-rich sulfide inclusions in early lamproite minerals. *Russian Geology and Geophysics, 44(9)*, 855-866.

Sparks, R. S. J., Baker, L., Brown, R. J., Field, M., Schumacher, J., Stripp, G., & Walters, A. (2006). Dynamical constraints on kimberlite volcanism. *Journal of Volcanology and Geothermal Research, 155*(1-2), 18-48.

Turner, S., Evans, P., & Hawkesworth, C. (2001). Ultrafast source-to-surface movement of melt at island arcs from ^{226}Ra-^{230}Th systematics. *Science, 292(5520)*, 1363-1366.

Turner, S., & Costa, F. (2007). Measuring timescales of magmatic evolution. *Elements, 3(4)*, 267-272.

Venturelli, G., Mariani, E. S., Foley, S. F., Capedri, S., & Crawford, A. J. (1988). Petrogenesis and conditions of crystallization of Spanish lamproitic rocks. *Canadian Mineralogist, 26*(pt 1), 67-79.

Wang, Z., Jin, Z., Mungall, J. E., & Xiao, X. (2020). Transport of coexisting Ni-Cu sulfide liquid and silicate melt in partially molten peridotite. *Earth and Planetary Science Letters, 536*, 116162.

Wilson, L., & Head, J. W. (2007). An integrated model of kimberlite ascent and eruption. *Nature, 447(7140*), 53-57.

Yao, Z., & Mungall, J. E. (2022). Transport and deposition of immiscible sulfide liquid during lateral magma flow. *Earth-Science Reviews, 227*, 103964.

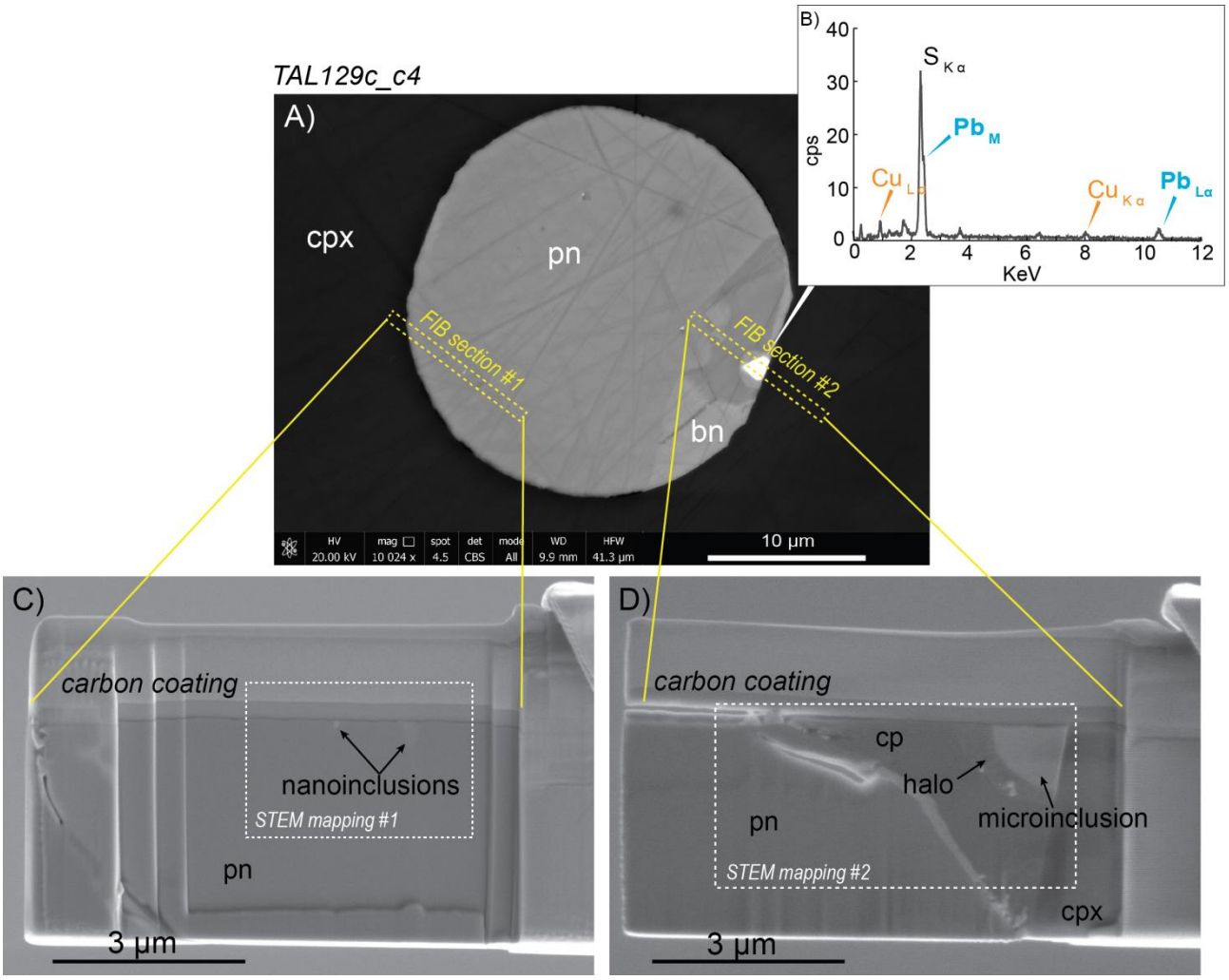

Supplementary Figure 1. Backscattered electron image (A), energy-dispersive X-ray spectroscopy spectrum (B) and corresponding electro transparent focused ion beam (FIB) sections (C, D) extracted from galena-bearing sulfide droplets in Tallante mantle xenolith (TAL129c). Ni-Fe peaks in EDS spectra in part are due to contamination by the host sulfide. pn—pentlandite; bn – bornite; cpx—clinopyroxene; cps—counts per second.

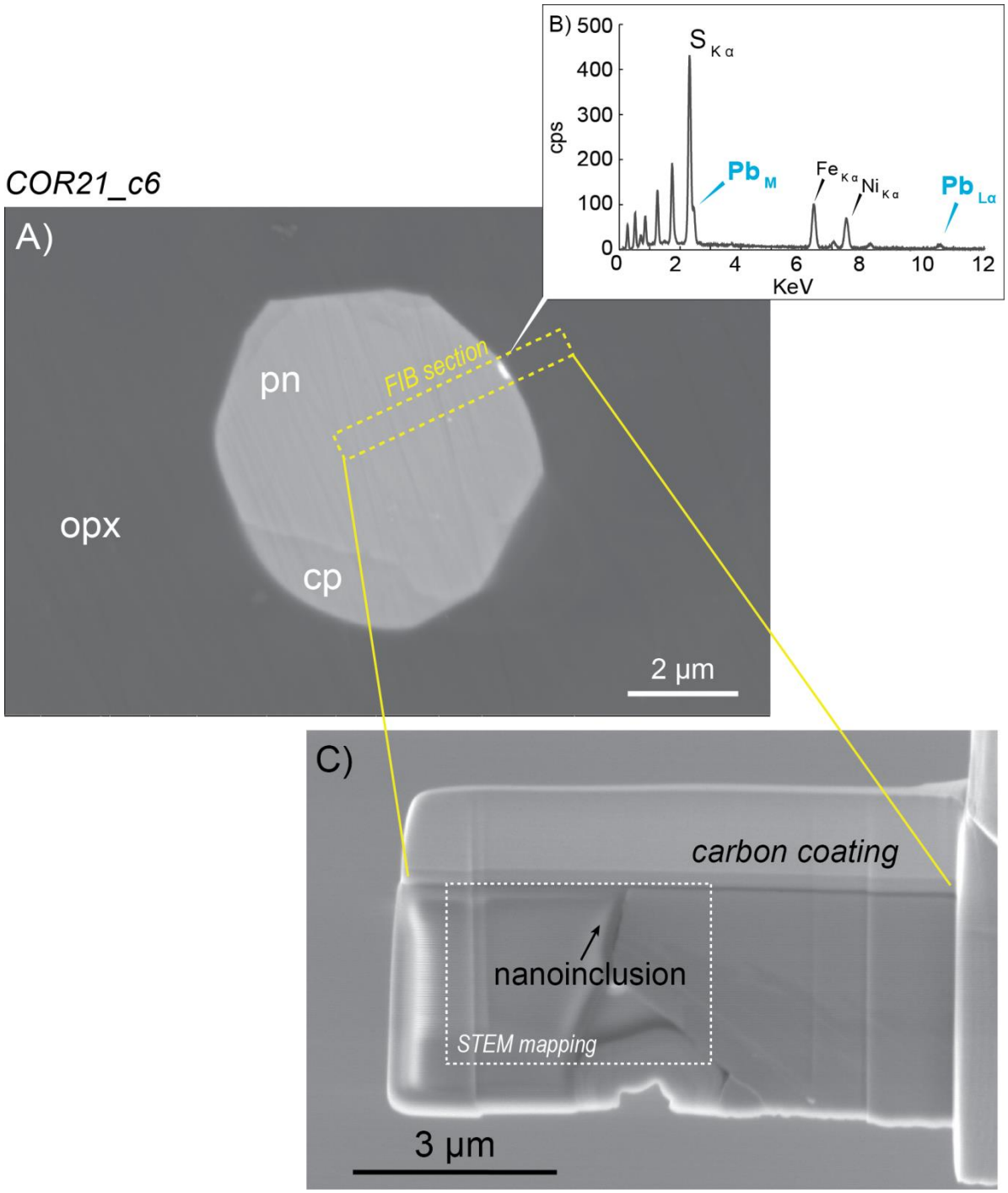

Supplementary Figure 2. Backscattered electron image (A), energy-dispersive X-ray spectroscopy spectrum (B) and corresponding electro transparent focused ion beam (FIB) section (C) extracted from galena-bearing sulfide droplets in Fortuna lamproite dyke (COR21_c6). Ni-Fe peaks in EDS spectra in part are due to contamination by the host sulfide. pn—pentlandite; cp – chalcopyrite; opx—orthopyroxene; cps—counts per second.

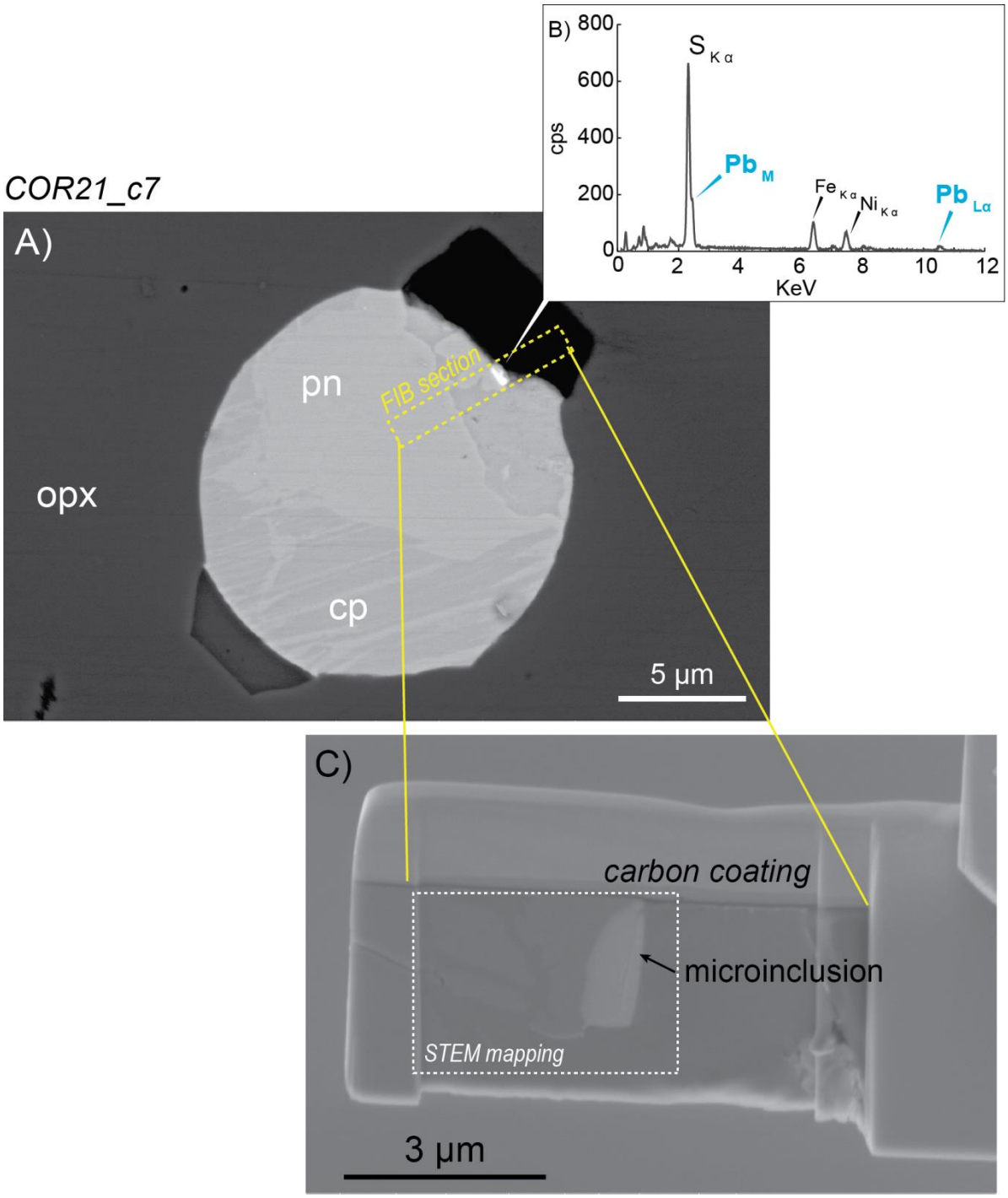

Supplementary Figure 3. Backscattered electron image (A), energy-dispersive X-ray spectroscopy spectrum (B) and corresponding electro transparent focused ion beam (FIB) section (C) extracted from galena-bearing sulfide droplets in Fortuna lamproite dyke (COR21_c7). Ni-Fe peaks in EDS spectra in part are due to contamination by the host sulfide. pn—pentlandite; cp – chalcopyrite; opx—orthopyroxene; cps—counts per second.

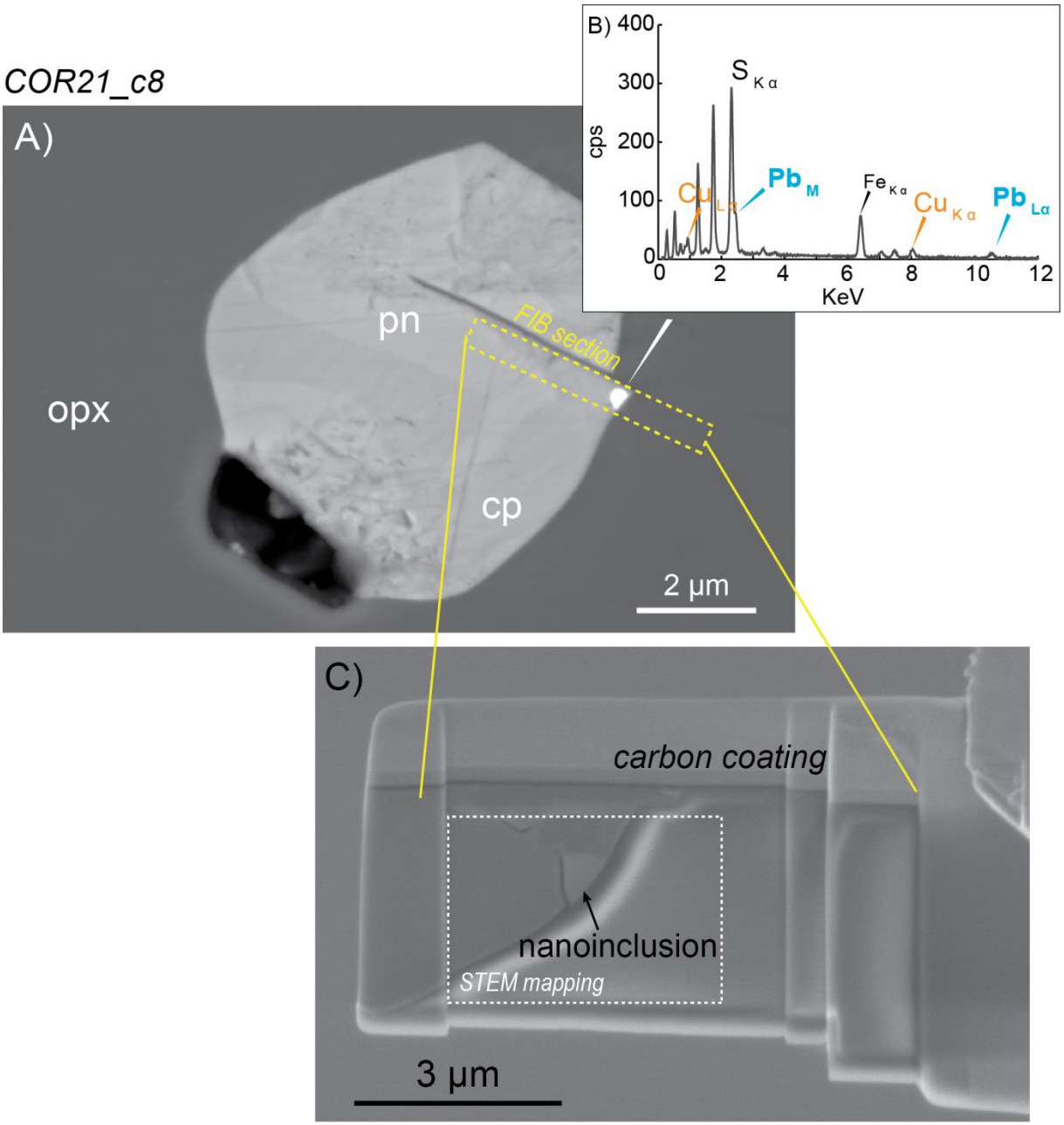

Supplementary Figure 4. Backscattered electron image (A), energy-dispersive X-ray spectroscopy spectrum (B) and corresponding electro transparent focused ion beam (FIB) section (C) extracted from galena-bearing sulfide droplets in Fortuna lamproite dyke (COR21_c8). Ni-Fe peaks in EDS spectra in part are due to contamination by the host sulfide. pn—pentlandite; cp – chalcopyrite; opx—orthopyroxene; cps—counts per second.

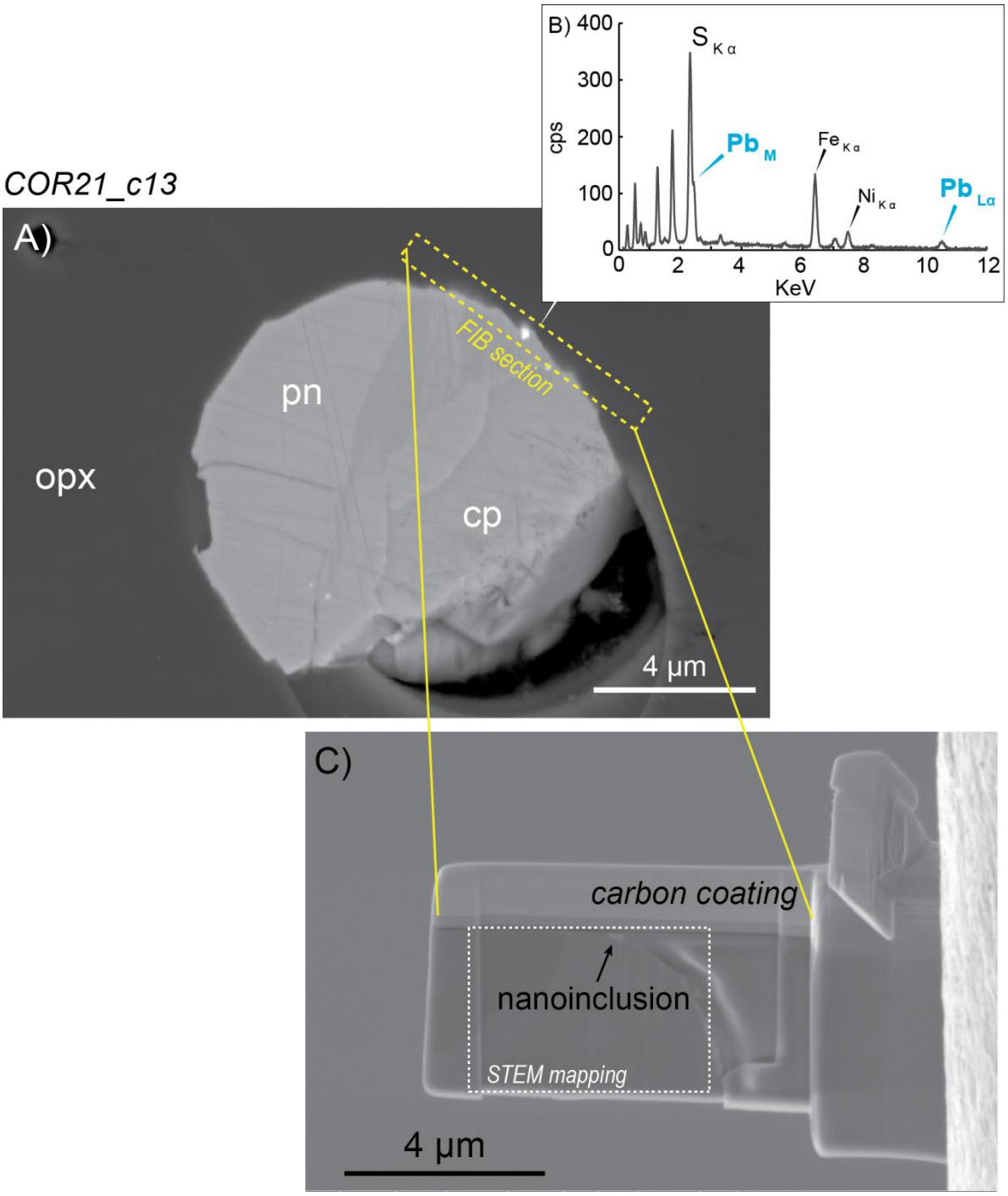

Supplementary Figure 5. Backscattered electron image (A), energy-dispersive X-ray spectroscopy spectrum (B) and corresponding electro transparent focused ion beam (FIB) section (C) extracted from galena-bearing sulfide droplets in Fortuna lamproite dyke (COR21_c13). Ni-Fe peaks in EDS spectra in part are due to contamination by the host sulfide. pn—pentlandite; cp – chalcopyrite; opx—orthopyroxene; cps—counts per second.

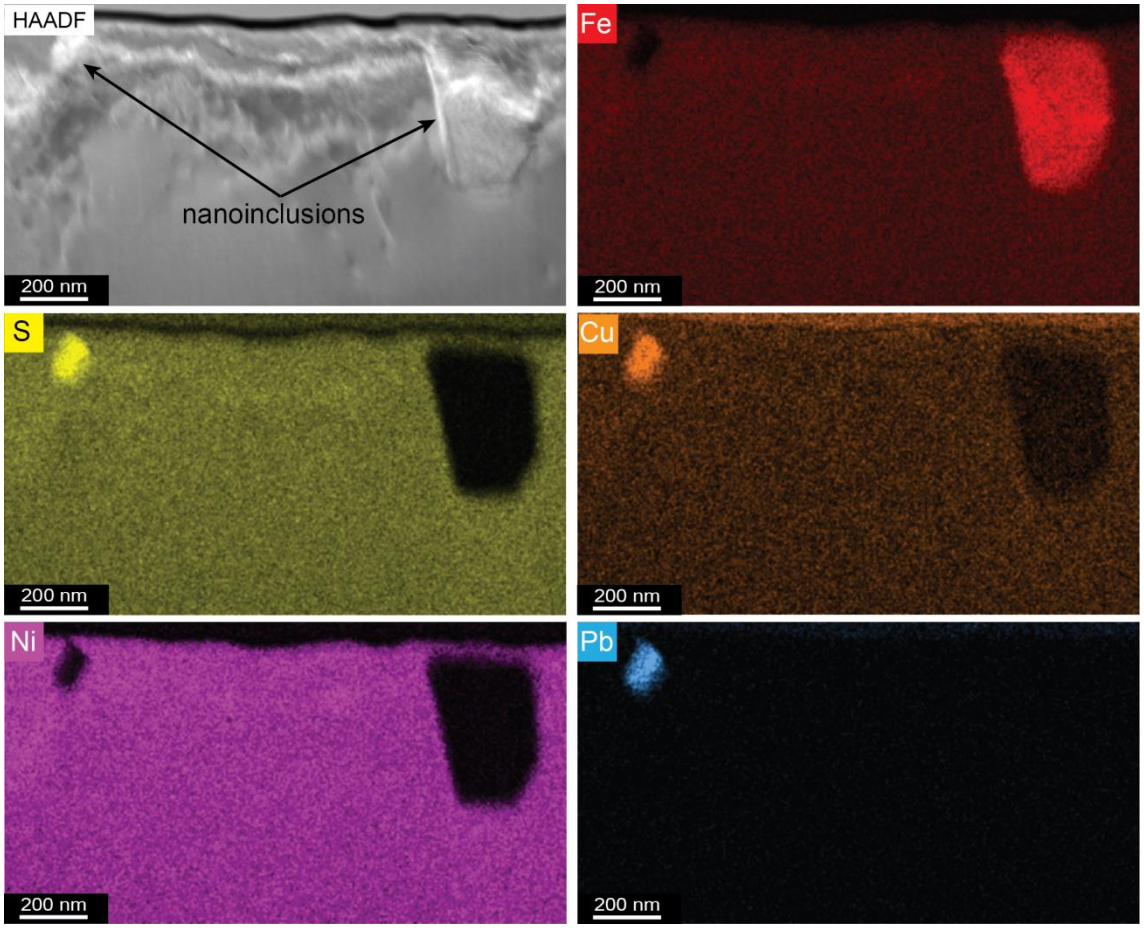

Supplementary Figure 6. High angle-annular dark field (HAADF) Z-contrast image and elemental maps in scanning transmission electron microscopy (STEM-EDS) acquired on TAL129_c4 thin foil sample by high resolution-transmission electron microscopy (HR-TEM).

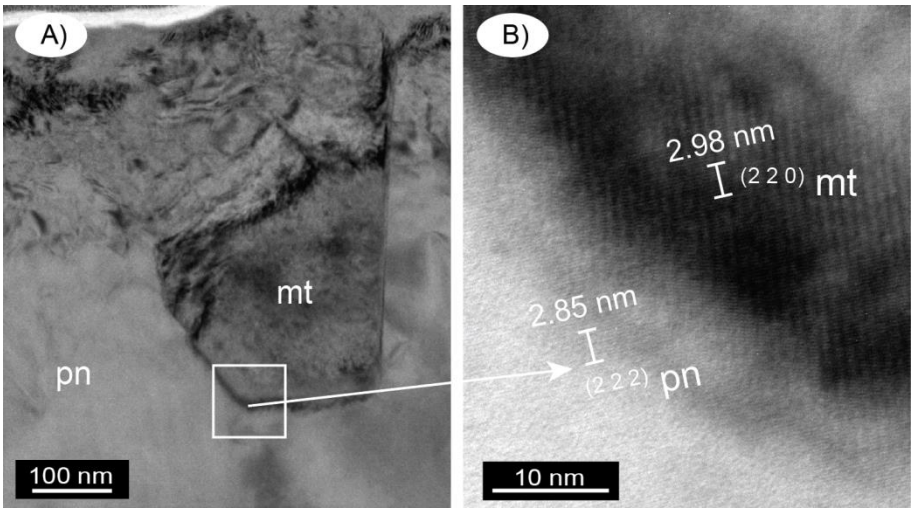

Supplementary Figure 7. Bright field scanning electron images (STEM; A) and high-resolution transmission electron microscopy images (HR-TEM; B) of magnetite nanoinclusion in thin foil sample TAL129c_c4.

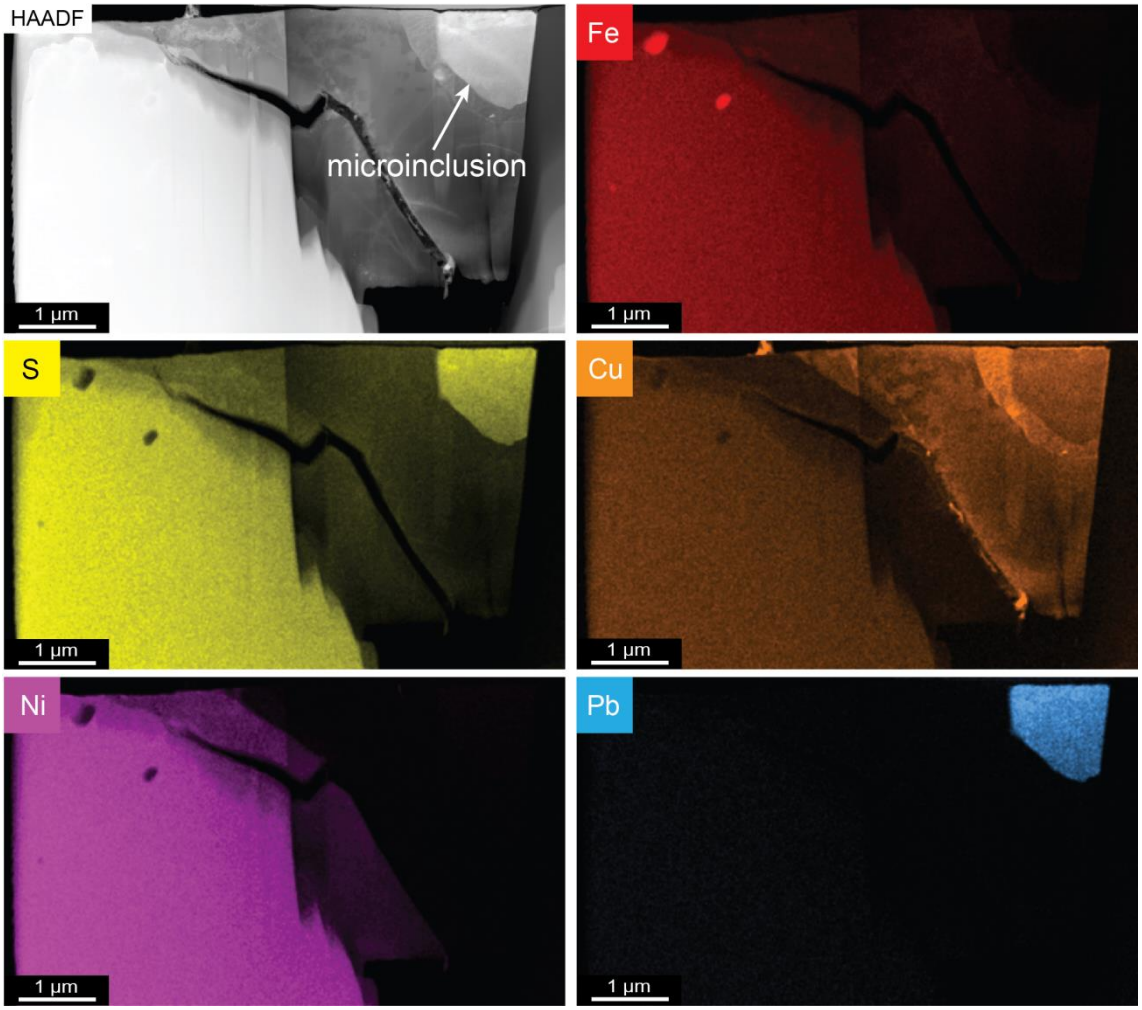

Supplementary Figure 8. High angle-annular dark field (HAADF) Z-contrast image and elemental maps in scanning transmission electron microscopy (STEM-EDS) acquired on TAL129_c4 thin foil sample by high resolution-transmission electron microscopy (HR-TEM).

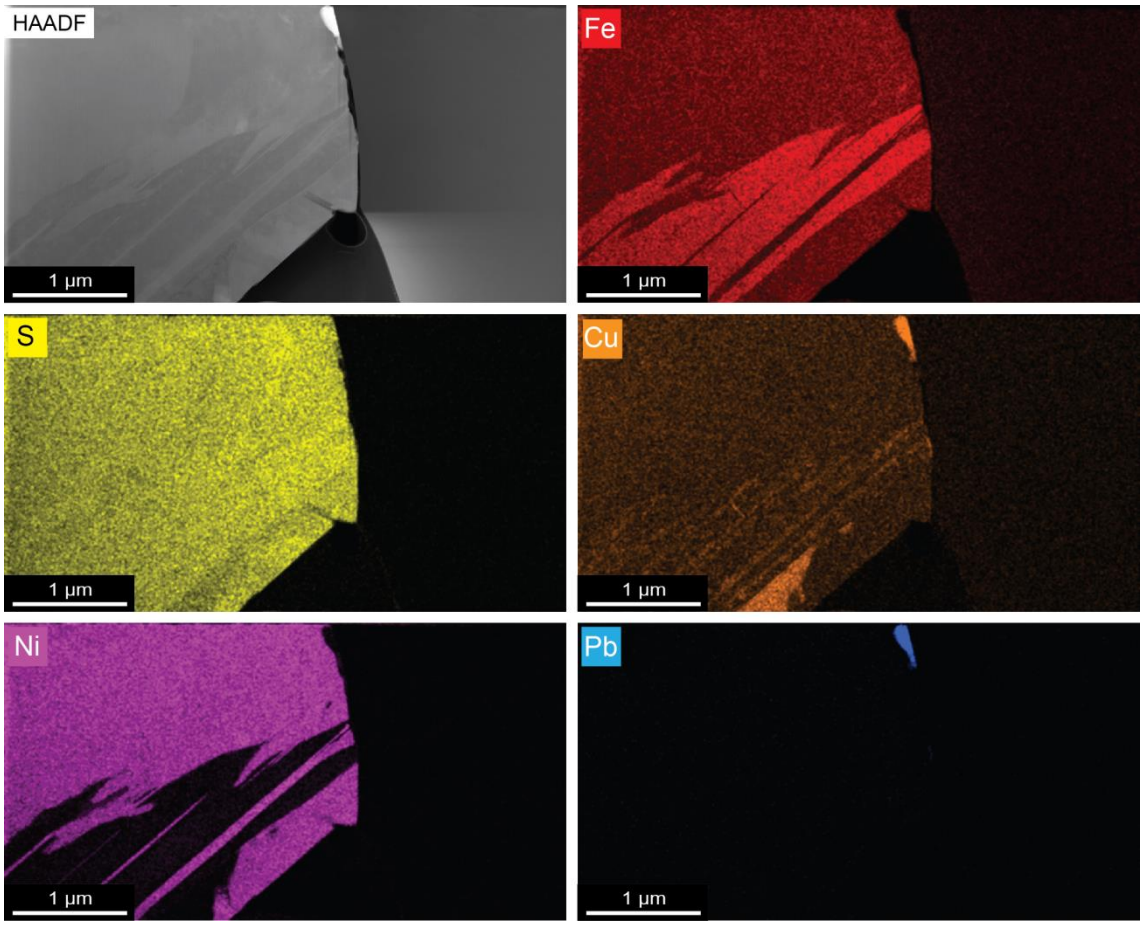

Supplementary Figure 9. High angle-annular dark field (HAADF) Z-contrast image and elemental maps in scanning transmission electron microscopy (STEM-EDS) acquired on COR21_c6 thin foil sample by high resolution-transmission electron microscopy (HR-TEM).

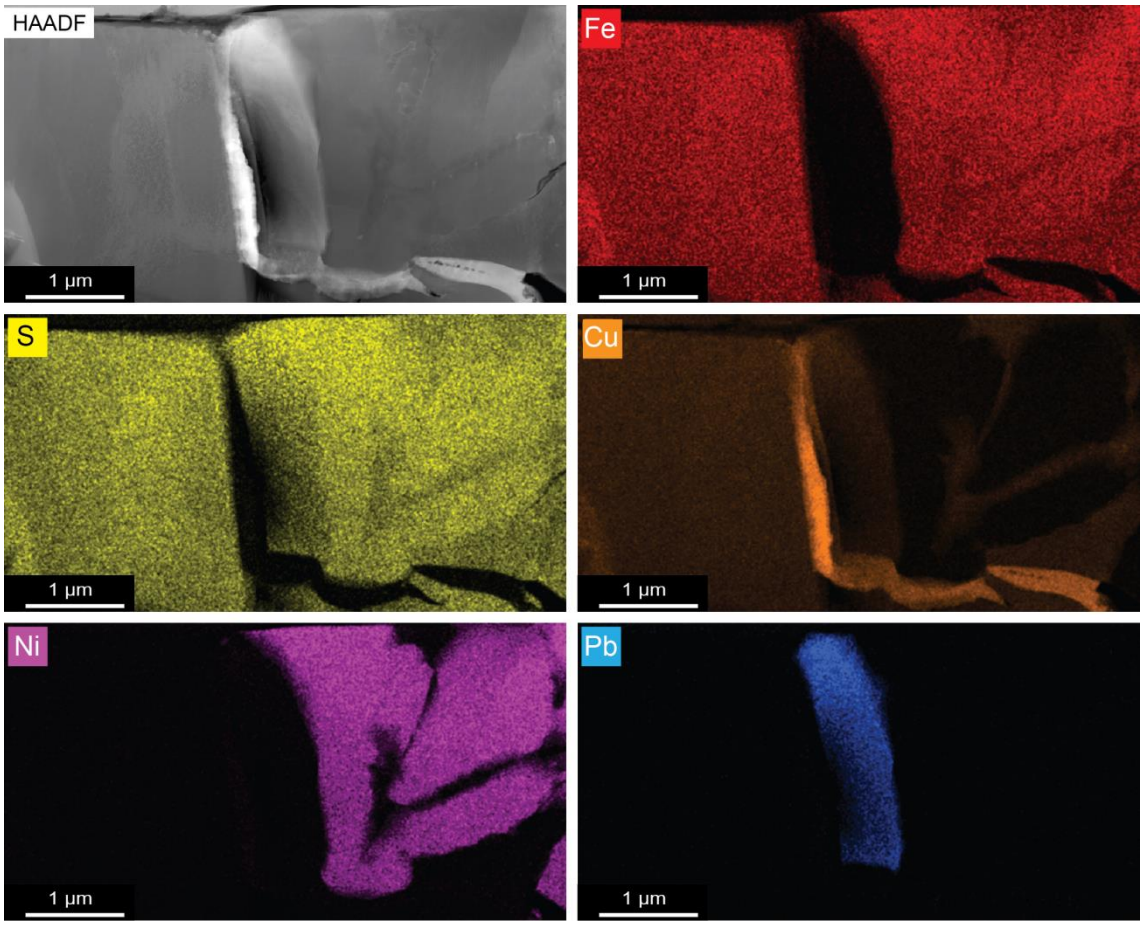

Supplementary Figure 10. High angle-annular dark field (HAADF) Z-contrast image and elemental maps in scanning transmission electron microscopy (STEM-EDS) acquired on COR21_c7 thin foil sample by high resolution-transmission electron microscopy (HR-TEM).

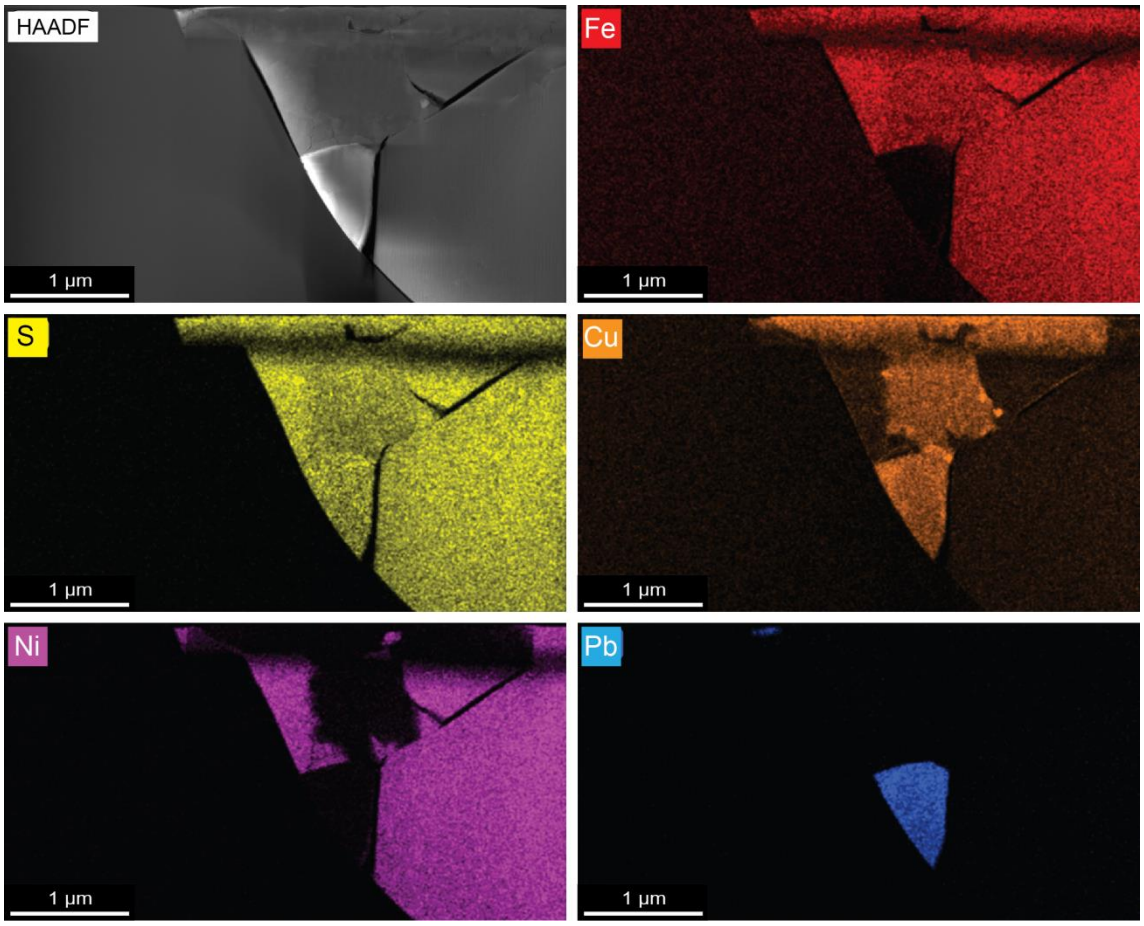

Supplementary Figure 11. High angle-annular dark field (HAADF) Z-contrast image and elemental maps in scanning transmission electron microscopy (STEM-EDS) acquired on COR21_c8 thin foil sample by high resolution-transmission electron microscopy (HR-TEM).

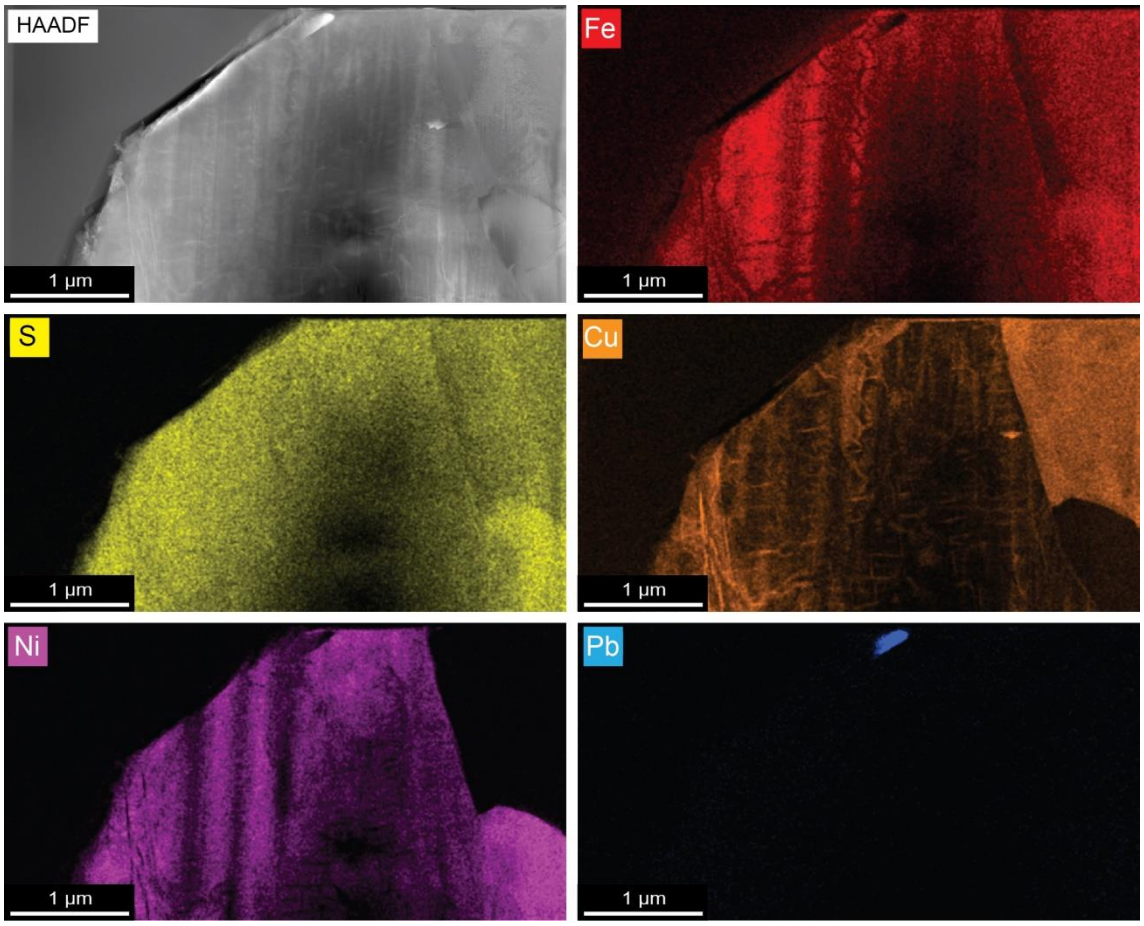

Supplementary Figure 12. High angle-annular dark field (HAADF) Z-contrast image and elemental maps in scanning transmission electron microscopy (STEM-EDS) acquired on COR21_c13 thin foil sample by high resolution-transmission electron microscopy (HR-TEM).

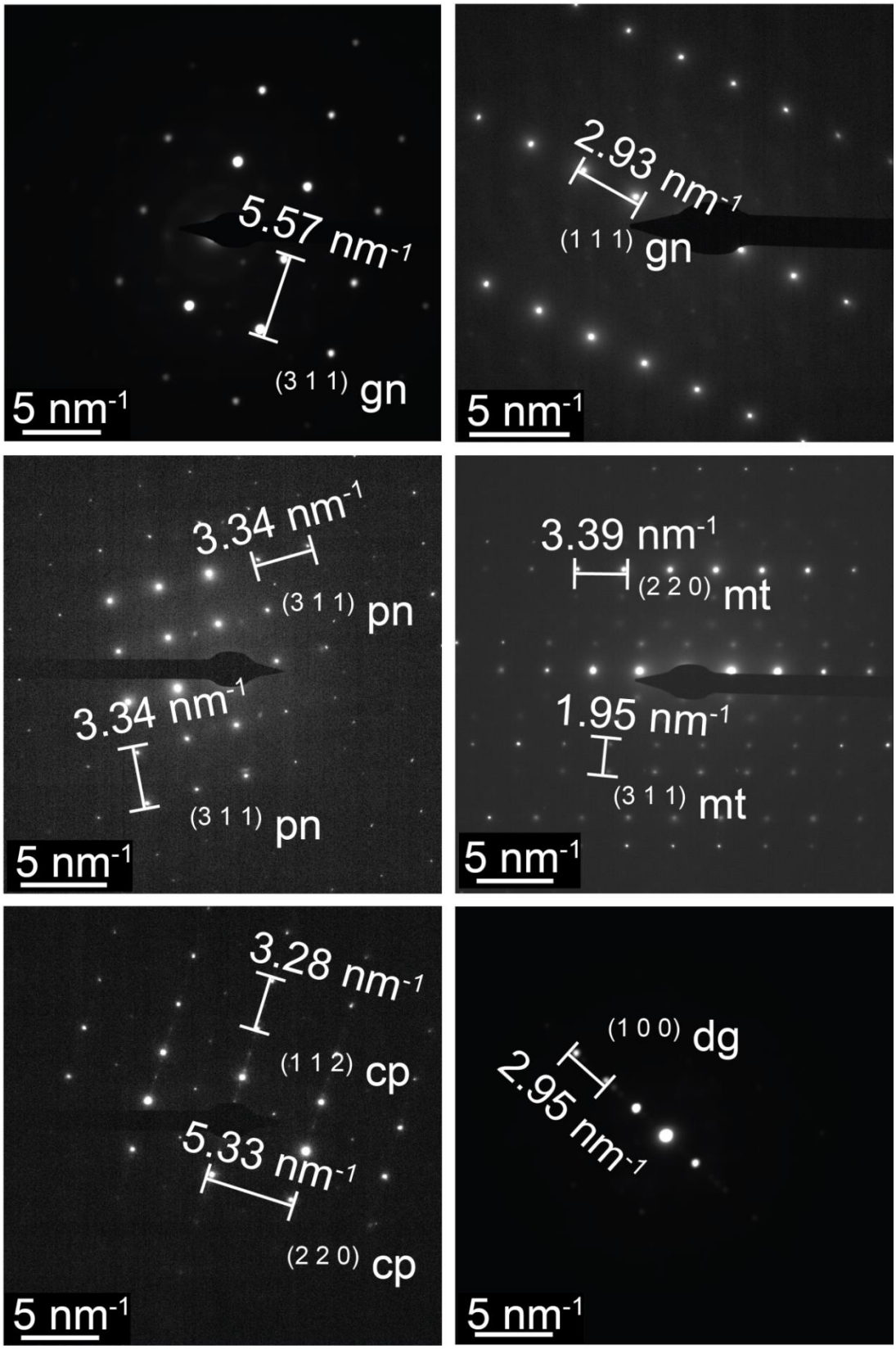

Supplementary Figure 13. Representative selected area electron diffraction (SAED) patterns and fast Fourier transform diffraction patterns from high resolution images of minerals identified in the Tallante peridotite xenoliths and Fortuna lamproite dykes. Abbreviations are: gn – galena; pn – pentlandite; mt – magnetite; cp – chalcopyrite; dg – digenite.